Supporting Information

Micropore engineering of biomass-derived carbon for durable, high-loading aqueous all-organic pouch batteries

Keisho Ri[ab], Nagihiro Haba[ab], Ryotaro Kumashiro[c], Ayaka Kido[ab], Tomoya Yamada[d], Yuto Katsuyama[e], Masaru Watanabe[d], Kayoko Kobayashi[f] and Yuta Nakayasu[adg]*

a. Frontier Research Institute for Interdisciplinary Sciences, Tohoku University, 6-3 Aoba, Aza, Aramaki, Aoba-ku, Sendai, Miyagi 980-8578, Japan. E-mail: nakayasu@tohoku.ac.jp

b. School of Engineering, Tohoku University, 6-6 Aoba, Aza, Aramaki, Aoba-ku, Sendai, Miyagi 980-8579, Japan.

c. Advanced Institute for Material Research, Tohoku University, Sendai 980-8577, Japan

d. Research Center of Supercritical Fluid Technology, Graduate School of Engineering Tohoku University 6-6-11, Aoba, Aza, Aramaki, Aoba-ku, Sendai, Miyagi 980-8579, Japan

e. Department of Chemistry & Biochemistry, University of California Los Angeles, Los Angeles, California, 90095-1569, USA

f. Division of Forest and Biomaterials Science, Graduate School of Agriculture, Kyoto University, Sakyo-ku, Kyoto 606-8502, Japan

g. Satoyama Engineering Co., Ltd, Matsubamoriyama 25-8, Maekawa, Shibata Gun Kawasaki Machi, Miyagi 989-1501, Japan

S1. Galvanostatic charge–discharge curves and combustion ion chromatography data

This section summarizes the galvanostatic charge–discharge (GCD) profiles and combustion ion chromatography data that were used to derive the specific capacities and quinone loadings listed in Table 1 of the main text. GCD measurements for TCBQ- and DCAQ-impregnated electrodes were performed at the 1 C rates defined in the Experimental section, corresponding to currents of 8.12 mA (0.0588 A g^{-1}) for TCBQ and 7.23 mA (0.0524 A g^{-1}) for DCAQ.

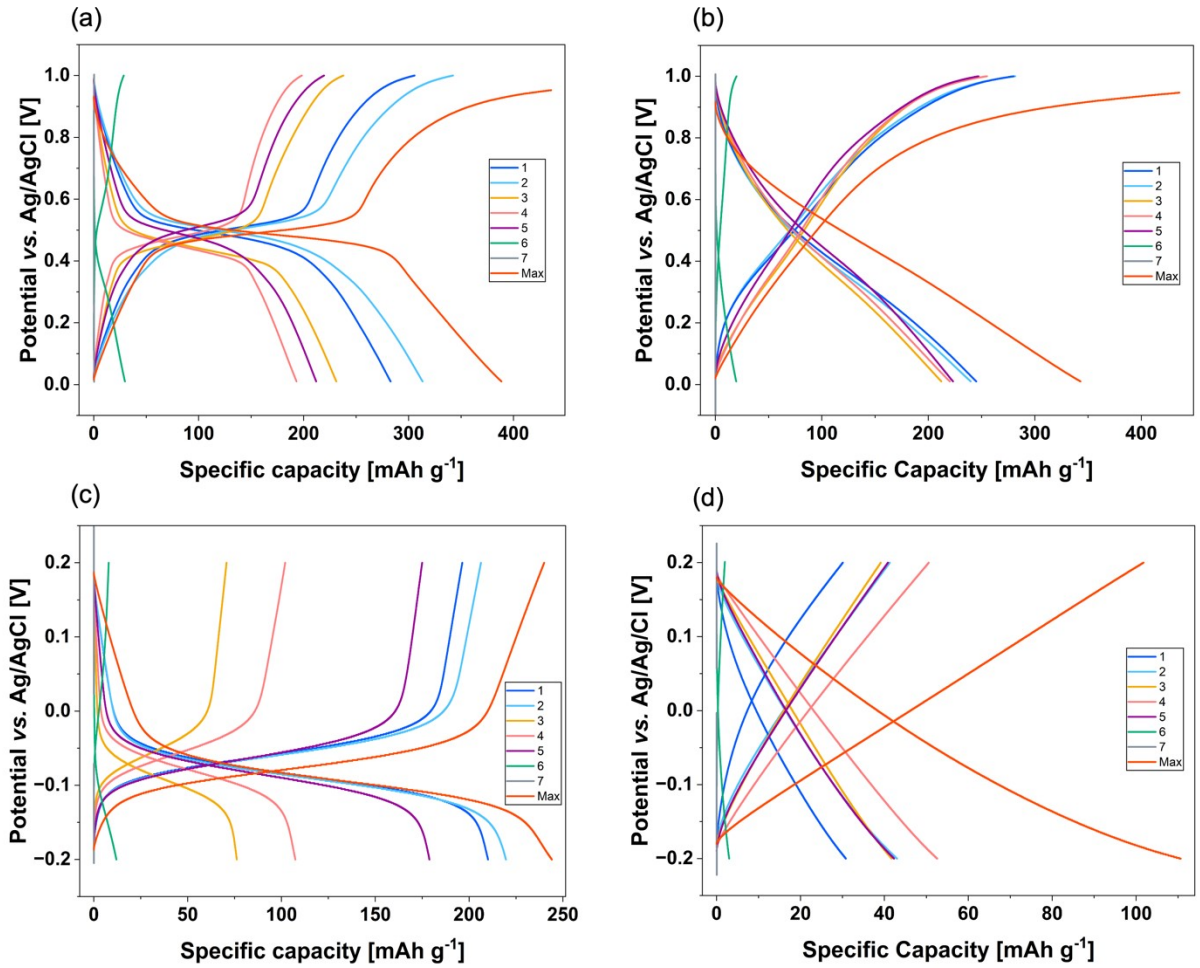

Fig. S1. Galvanostatic charge–discharge (GCD) curves of TCBQ- and DCAQ-impregnated and blank activated carbon electrodes in three-electrode half cells. (a) GCD curves of TCBQ-impregnated electrodes. (b) GCD curves of pristine (blank) activated carbon electrodes measured over the same potential window and at the same current as the TCBQ-impregnated electrodes in (a). (c) GCD curves of DCAQ-impregnated electrodes. (d) GCD curves of pristine (blank) activated carbon electrodes measured over the same potential window and at the same current as the DCAQ-impregnated electrodes in (c).

Table S1. Chlorine contents (Cl wt%) of TCBQ- and DCAQ-impregnated electrodes determined by combustion ion chromatography.

Sample	Cl [wt%]– TCBQ	Cl [wt%]– DCAQ
1	15	7.4
2	15	7.0
3	17	8.8
4	15	7.0
5	16	7.1
6	9.1	8.1
7	13	7.5
Max	15	7.4

S2. CO_2 adsorption-derived pore size distributions of activated carbons

This section provides the pore size distributions (PSDs) obtained from CO_2 adsorption isotherms at 273 K for the pristine activated carbons. The PSDs were calculated as described in the Experimental section. For each sample, the pore volume was integrated over selected micropore windows, including the 0.7–0.8 nm range that showed the strongest correlation with the TCBQ and DCAQ redox capacities in **Fig. 2** of the main text.

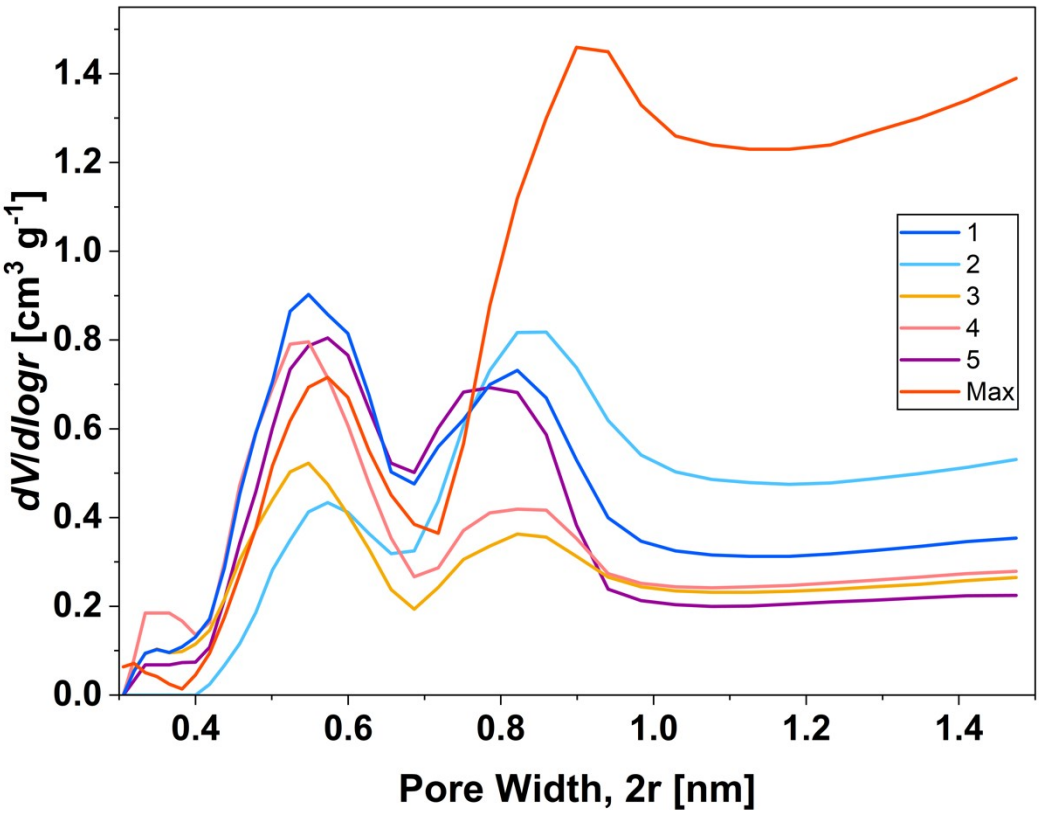

Fig S2. Pore size distribution (PSD) of the pristine activated carbon hosts, derived from CO_2 adsorption isotherms. The PSDs were obtained from CO_2 adsorption measurements prior to quinone impregnation, and the micropore region around 0.7–0.8 nm is used for the capacity correlation analysis discussed in the main text.

Table S2. Micropore volumes derived from CO_2 adsorption for selected pore-width windows. Pore Volume of 0.7–0.8 nm denotes the pore volumes integrated over the 0.7–0.8 nm windows.

Sample	Pore Volume of 0.7–0.8 nm [$cm^3\ g^{-1}$]
1	0.03723
2	0.03262
3	0.01665
4	0.02048
5	0.03526
Max	0.03243

S3. N_2 adsorption-derived pore size distributions of activated carbons

This section provides the pore size distributions (PSDs) obtained from N_2 adsorption isotherms at 77 K for the pristine activated carbons and the commercial reference Maxsorb®. The PSDs were calculated using the Barrett–Joyner–Halenda (BJH) method applied to the desorption branch of the isotherms, as described in the Experimental section. While the main text focuses on the ultramicropore region (< 1 nm) probed by CO_2, which governs the ion confinement capacity, these N_2-derived distributions characterize the larger mesoporous channels relevant to bulk electrolyte transport. **Fig S3** presents the full dataset, including Sample 4 and Maxsorb®, to provide a complete overview of the pore structures across the synthesized and reference materials.

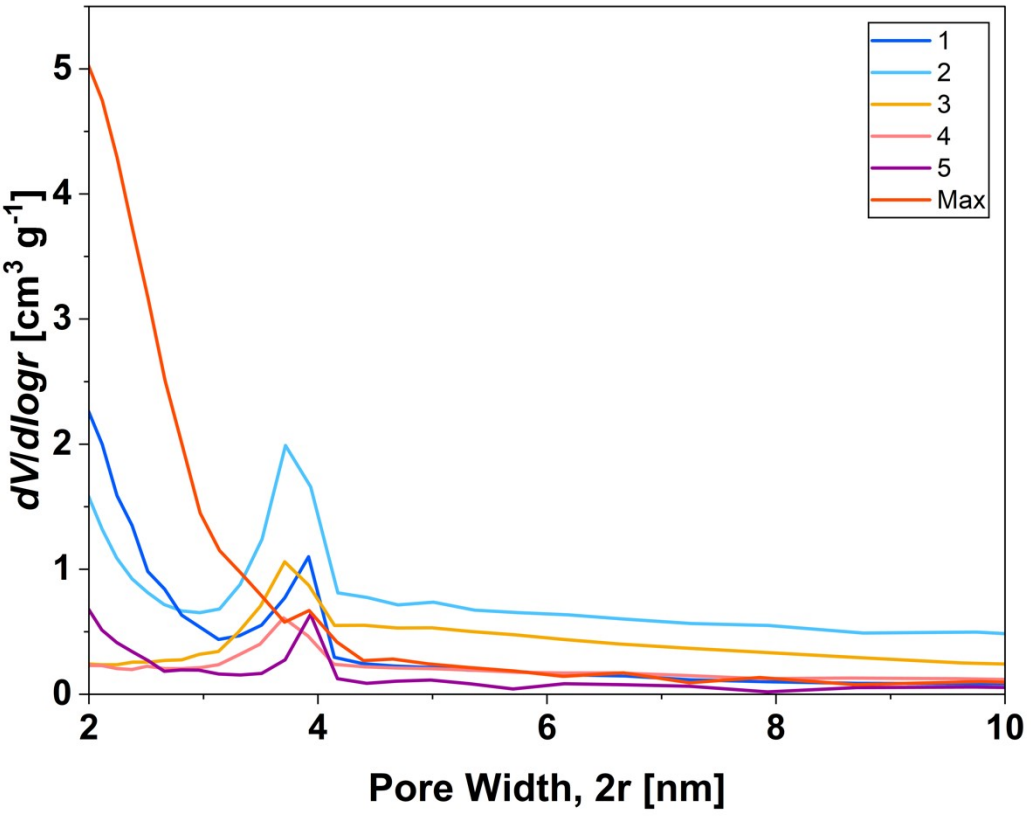

Fig S3. BJH pore size distributions derived from N_2 desorption isotherms for all activated carbon samples (Samples 1–5) and the reference Maxsorb®. The data for Samples 1, 2, 3, and 5 correspond to those discussed in the main text, while Sample 4 and Maxsorb® are shown here for completeness.

S4. Molecular dimensions of TCBQ and DCAQ obtained from DFT-optimized structures

Molecular geometries of TCBQ (tetrachloro-1,4-benzoquinone) and DCAQ (1,5-dichloroanthraquinone) were optimized using density functional theory (DFT) as implemented in Gaussian 16. Geometry optimizations were carried out at the B3LYP/6-31G(d) level of theory with Grimme's D3 dispersion correction with Becke–Johnson damping (D3(BJ)).

Table S3. Geometric dimensions of TCBQ and DCAQ obtained from DFT-optimized structures. Long axis and Short axis denote the in-plane long and short molecular axes of the quinone core including chloro substituents, respectively, while Thickness represents the molecular extent normal to the least-squares plane of the aromatic core.

	Long axis [nm]	**Short axis [nm]**	**Thickness [nm]**
TCBQ	0.992	0.843	0.350
DCAQ	1.200	0.970	0.350

S5. Thickness-dependent EIS and current-collector architecture effects in pouch cells

Electrochemical impedance spectroscopy (EIS) was measured for TCBQ cathode electrodes with different single-sided film thicknesses (0.25, 0.50, 1.00, and 1.50 mm). Measurement conditions are described in the Experimental section. Nyquist plots for electrodes with different film thicknesses are shown in **Fig. S5**. The curves represent the raw impedance data connected as displayed in ZView (no fitted curves are overlaid). For quantitative comparison, only the high-frequency depressed semicircle region was analyzed using an equivalent circuit Rs (CPE || Rp) in ZView, where Rs is the series resistance and Rp corresponds to the semicircle width (taken as $R_{ct,\ app}$). The CPE parameters are reported as Y_0 (CPE-T) and α (CPE-P). In addition, $Y_{0,\ est}$ was estimated as $Y_0 = 1/(R_{ct,\ app}\ \Omega_{max}{}^{\alpha})$, where $\Omega_{max}=2\pi f_{max}$ and f_{max} is the frequency at the apex of the semicircle (-Z'' maximum). The extracted parameters are summarized in **Table S4**.

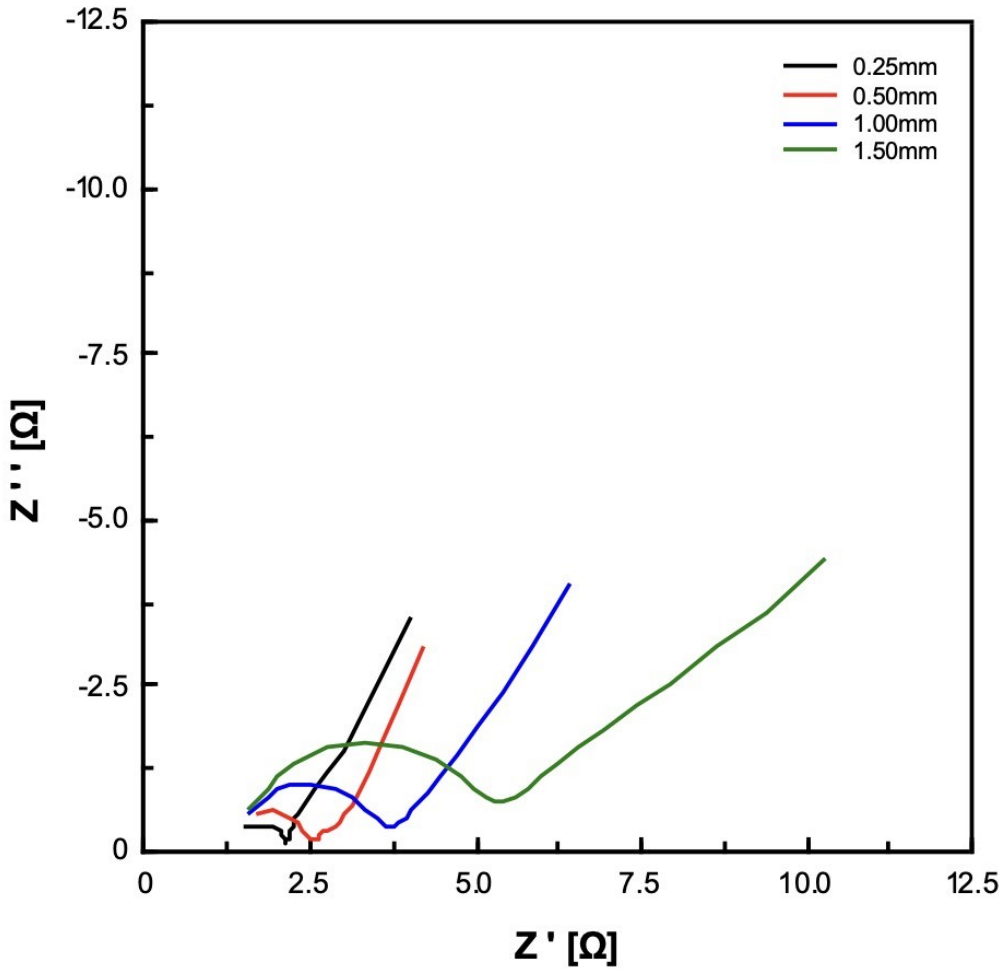

Fig. S5. Thickness-dependent EIS of TCBQ cathode electrodes. Nyquist plots for electrodes with single-sided film thicknesses of 0.25, 0.50, 1.00, and 1.50 mm measured under identical conditions.

Table S4. Fitted EIS parameters for electrodes with different thicknesses. Parameters were obtained by fitting the high-frequency depressed semicircle using the equivalent circuit Rs (CPE || Rp). Measurement conditions are described in the Experimental section. Rp corresponds to the apparent polarization resistance.

Thickness [mm]	Rs [Ω]	Rp [Ω]	$Y_{0,\,est}$ [Ω^{-1} s^{α}]	α
0.25	1.259	0.89313	0.00024274	0.9592
0.50	0.79377	1.837	0.00091582	0.72624
1.00	0.67813	3.255	0.00176691	0.68483
1.50	1.007	4.653	0.00085257	0.77759

In addition, 1C galvanostatic charge–discharge (GCD) profiles of large-area pouch cells are compared for designs with and without a stainless-steel current-bus.

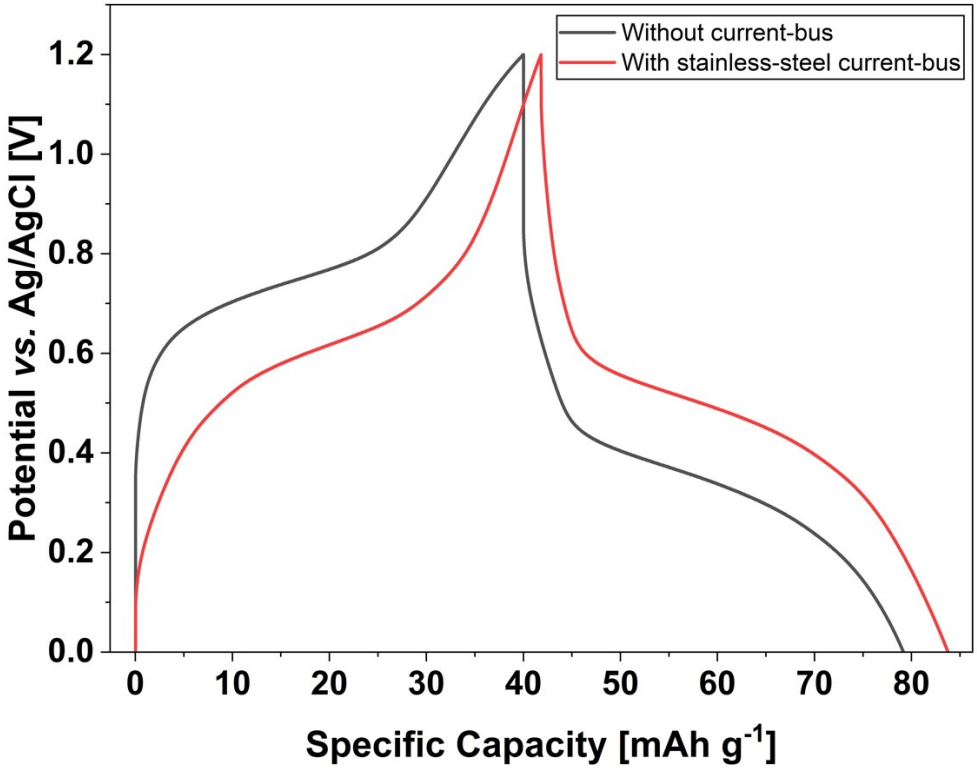

Fig. S6. Pouch-cell GCD at 1C with and without a stainless-steel current-bus. Galvanostatic charge–discharge curves comparing bus-integrated and bus-free pouch-cell designs at 1C. Curves are shown for the 2nd cycle.

S6. Electrolyte-volume-limited dissolution analysis, combustion ion chromatography (ClC) results, and N_2-bubbling experiment

This section provides the detailed calculation procedure used for the electrolyte-volume-limited dissolution analysis described in the main text. We assumed that dissolution of the reduced species, tetrachloro-1,4-hydroquinone (TCHQ), is the dominant mass-loss pathway for TCBQ during cycling. The maximum amount of TCHQ that can dissolve is limited by its solubility and the electrolyte volume.

As an upper bound, we used the aqueous solubility of TCHQ at 25 °C, S_{TCHQ} = 76 mg L^{-1}. This value was applied to the 0.5 M H_2SO_4 electrolyte, even though salting-out effects are expected to decrease the solubility; therefore, the calculated values represent conservative upper limits. For a given cell, the maximum dissolved mass $m_{diss,max}$ is

$$m_{diss,max} = S_{TCHQ} \times V$$

where V is the electrolyte volume. The corresponding maximum loss fraction f_{max} relative to the initial TCBQ inventory m_{TCBQ} in the electrodes is

$$f_{max} = m_{diss,max} / m_{TCBQ}$$

For the beaker cell, the electrolyte volume was approximately $V \approx$ 120 mL (= 0.120 L), giving

$$m_{diss,max,beaker} = 76\ mg\ L^{-1} \times 0.120\ L = 9.12\ mg$$

The initial TCBQ mass in the tested beaker-cell electrode was $m_{TCBQ,beaker}$ = 32.17 mg, so the maximum loss fraction is

$$f_{max,beaker} = 9.12\ mg / 32.17\ mg \approx 0.245\ (\approx 24.5\%)$$

For the pouch cell, the electrolyte volume was much smaller ($V \approx$ 15 mL = 0.015 L), while the total TCBQ inventory was larger ($m_{TCBQ,\ pouch} \approx$ 425 mg). In this case,

$$m_{diss,max,pouch} = 76\ mg\ L^{-1} \times 0.015\ L = 1.14\ mg$$

and the corresponding maximum loss fraction is

$$f_{max,\ pouch} = 1.14\ mg / 425\ mg \approx 2.7 \times 10^{-3}\ (\approx 0.27\%)$$

These numerical values were used to obtain the upper bounds $f_{max,beaker}$ and $f_{max,pouch}$ discussed in the main text, where they are compared with the experimentally observed capacity fade fractions f_{obs} (**Fig. 3b** and **Fig. 5b**).

Optionally, these results can be summarized as follows:

- Beaker cell: V = 120 mL, m_{TCBQ} = 32.17 mg, $m_{diss,max}$ = 9.12 mg, $f_{max,beaker} \approx$ 28.3%.
- Pouch cell: V = 15 mL, m_{TCBQ} = 425 mg, $m_{diss,max}$ = 1.14 mg, $f_{max,pouch} \approx$ 0.27%.

To provide additional experimental support for electrolyte-mediated mass transfer, chlorine in the post-2000cycles-test electrolyte (0.5 M H_2SO_4) was quantified by combustion ion chromatography (CIC). **Table S5** summarizes the measured chlorine levels reported as the elemental chlorine mass fraction (Cl, wt%) in the analyzed electrolyte aliquots. Assuming a solution density of ~1 g mL^{-1}, the measured values (0.005–0.007 wt%) correspond to ~50–70 mg L^{-1} as Cl (average ~ 60 mg L^{-1}).

As a conservative, assumption-based reference conversion, we estimated the potential dissolved masses of organochlorine redox species by assuming that (i) the detected chlorine predominantly reflects dissolved organochlorine molecules originating from the redox-active species and (ii) the dissolved reduced species from the TCBQ and DCAQ couples are present at a 1:1 molar ratio. Under these assumptions, the average chlorine level corresponds to ~70 mg L^{-1} of TCHQ and ~79 mg L^{-1} of reduced DCAQ (anthrahydroquinone), i.e., ~149 mg L^{-1} in total. This gives estimated dissolved masses of ~8.39 mg (TCHQ) + ~9.44 mg ($DCAQ_{red}$) for the beaker cell (0.120 L) and ~1.05 mg (TCHQ) + ~ 1.18 mg ($DCAQ_{red}$) for the pouch cell (0.015 L). Converting these masses to capacity-loss equivalents using the theoretical capacities (218 mAh g^{-1} for TCBQ and 194 mAh g^{-1} for DCAQ) yields a reference estimate of ~22–24% for the beaker cell and ~0.22–0.25% for the pouch cell. These values are consistent with the experimentally observed capacity decreases (beaker: ~23%; pouch: ~0.25%), suggesting that electrolyte-mediated mass transfer could plausibly contribute to the long-term capacity loss in the beaker configuration, whereas its contribution is intrinsically limited in the pouch cell due to the much smaller electrolyte volume.

We emphasize that the above conversion from chlorine to dissolved organochlorine mass is provided as a conservative supporting estimate under explicit assumptions (e.g., 1:1 molar ratio of dissolved reduced species). The solubility-based upper-bound framework using S_{TCHQ} remains the primary basis for the electrolyte-volume-limited dissolution analysis.

Table S5. Sample weight and elemental composition (Cl and S wt%) of electrolyte aliquots determined by combustion ion chromatography (CIC).

Sample mass [mg]	Cl [wt%]	S [wt%]
6.7253	0.005	1.82
5.9046	0.007	1.86

To experimentally probe dissolution-driven degradation under conditions similar to the beaker cell, we performed a two-week N_2 bubbling experiment. In this test, the electrolyte in a beaker cell (0.5 M H_2SO_4) was continuously bubbled with N_2 for approximately two weeks, with periodic replenishment of the evaporated solvent to maintain the nominal electrolyte volume. After this pre-treatment, galvanostatic charge–discharge (GCD) measurements were carried out using fresh electrodes and the N_2-bubbled electrolyte under the same conditions as the baseline beaker-cell experiments. Compared with the baseline electrolyte, the N_2-bubbled electrolyte led to a capacity decrease of roughly 20% after extended cycling, consistent with the long-term fade observed in the beaker configuration (**Fig. 3b** in the main text). Together with the electrolyte-volume-limited upper-bound analysis and the detection of chlorine in the post-test electrolyte (**Table S5**), these results support the view that electrolyte-mediated mass transfer (including dissolution of reduced organochlorine redox species) can contribute substantially to the long-term capacity loss under beaker-cell conditions with a large electrolyte volume.

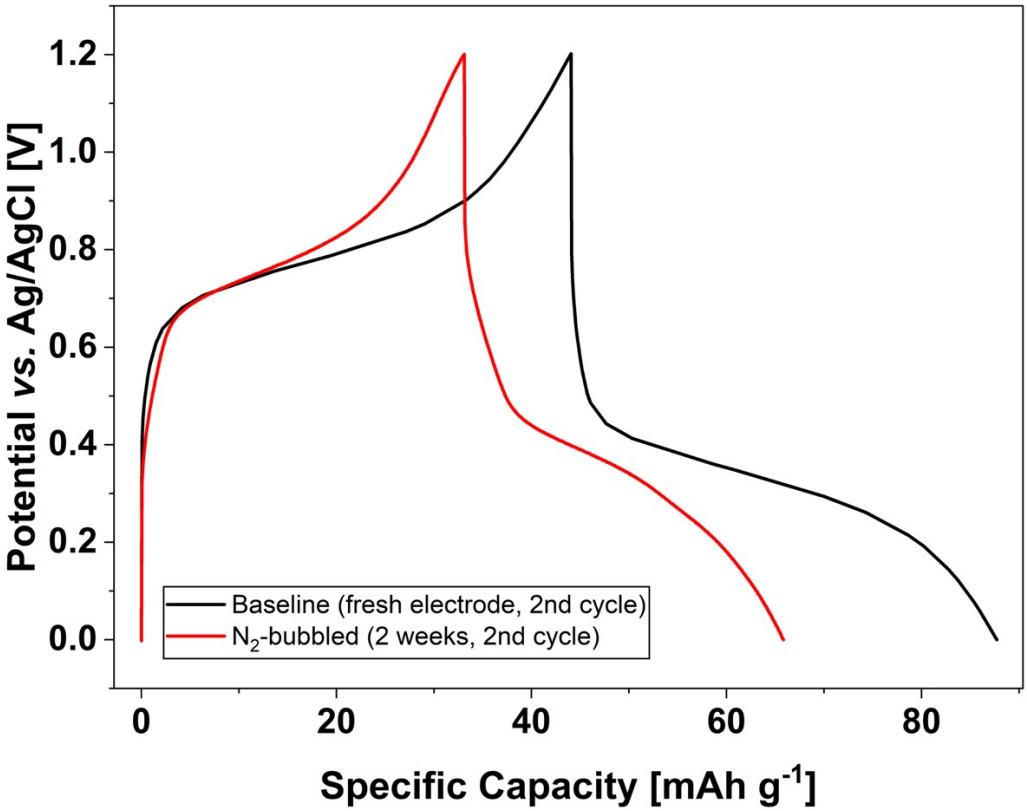

Fig. S7. Galvanostatic charge–discharge (GCD) curves of TCBQ-impregnated electrodes in beaker cells using the baseline electrolyte (black) and the electrolyte after two weeks of N_2 bubbling (red). Both measurements were performed under identical current and potential-window conditions as in the beaker-cell tests described in the main text.

S7. High-q WAXS parameterization for apparent profile descriptors

WAXS patterns of the impregnated electrodes were analyzed to obtain apparent descriptors of the high-*q* profile shape associated with short-range electron-density heterogeneity in the carbon–quinone composites. The azimuthally integrated intensity $I(q)$ was expressed as a function of the magnitude of the scattering vector, $q = 4\pi \sin\theta/\lambda$, and the data were normalized by transmitted intensity and sample thickness to enable quantitative comparison between samples. Owing to the structural heterogeneity of activated-carbon pore networks and the non-negligible background contribution in the high-q region, a rigorously defined Guinier regime could not be identified in the present data. Therefore, the Guinier-type treatment applied here was not used for absolute size determination.

$$\ln I(q) = \ln I_0 - (R_{app}^2/3)q^2$$

where $I(q)$is the scattering intensity at scattering vector q, and $R_{app}$is a formal fitting parameter obtained from the slope of the linear regression. Importantly, R_{app}here is not interpreted as a physical radius of gyration in the conventional Guinier sense. Rather, it serves only as an apparent descriptor of the high-q profile shape within the selected fitting window. An apparent descriptor $d$was then defined as:

$$r = \sqrt{5/3}\, R_{app}$$

This relation is adopted formally for consistency with conventional Guinier-type parameterization, but no physical meaning as a pore diameter, structural domain size, or rigorous electron-density correlation length is assigned.

q-window definition

For each molecular series (TCBQ and DCAQ), a common q-window was predefined and applied unchanged to all samples within that series. No sample-specific optimization of the fitting window was performed. Linear least-squares fits were carried out within this fixed window solely to generate formal apparent descriptors of the high-q profile shape. Because the numerical values of $R_g$and $d$can depend on background treatment and window selection, and because no strict Guinier regime is established, the resulting parameters are used only for qualitative within-series comparison. No unique structural size is inferred from these values.

Symbols (WAXS)

- $I(q)$: azimuthally integrated scattering intensity.
- q (nm^{-1}): magnitude of the scattering vector, $q = 4\pi \sin\theta/\lambda$.

- R_{app} (nm): apparent R_{app}-like fitting parameter obtained from Guinier-type linearization of the selected high-*q* region.
- r (nm): apparent derived descriptor, calculated as $r = \sqrt{5/3}R_{app}$.
- d (nm): apparent derived descriptor, calculated as $d = 2r$, used only for relative comparison within this dataset.

Table S6. Apparent descriptors obtained from Guinier-type linearization of high-q WAXS profiles

Sample	*q*-window (TCBQ) [nm^{-1}]	r (TCBQ) [nm]	*d* (TCBQ) [nm]	*q*-window (DCAQ) [nm^{-1}]	*r* (DCAQ) [nm]	*d* (DCAQ) [nm]
1	7.02–10.00	0.306	0.612	4.80–6.99	0.418	0.836
2	7.02–10.00	0.340	0.680	4.80–6.99	0.423	0.846
3	7.02–10.00	0.402	0.804	4.80–6.99	0.230	0.460
4	7.02–10.00	0.427	0.854	4.80–6.99	0.244	0.488
5	7.02–10.00	0.405	0.810	4.80–6.99	0.383	0.766
Max	7.02–10.00	0.334	0.668	4.80–6.99	0.450	0.900

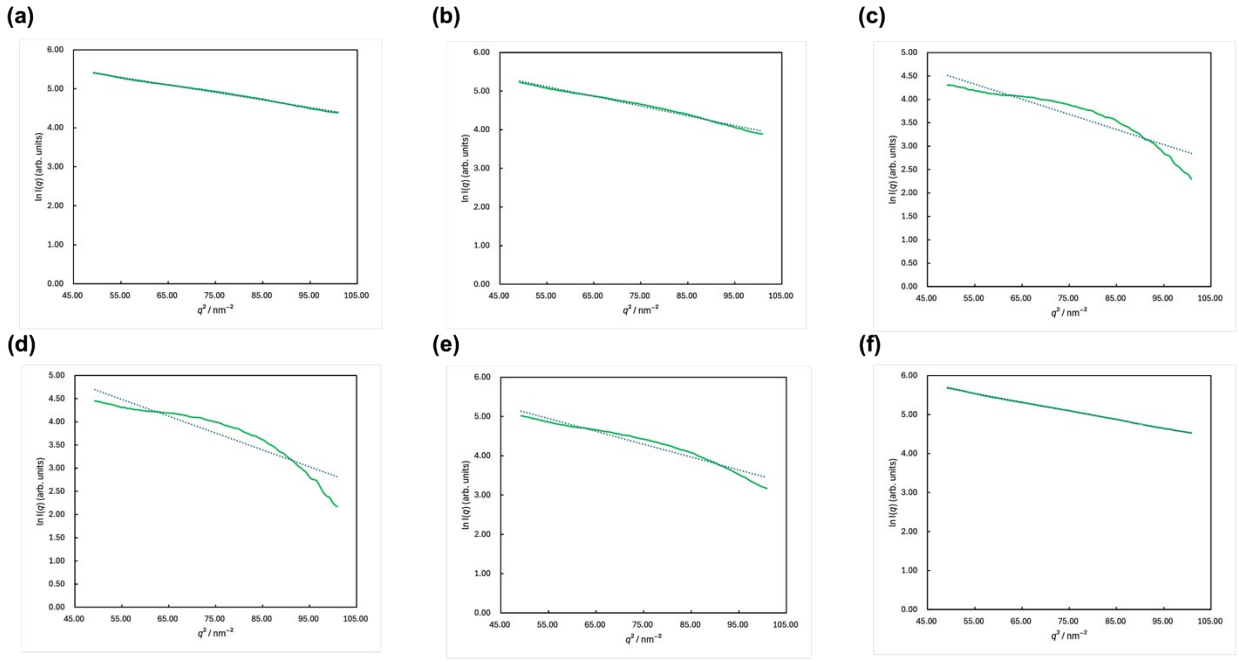

Fig. S8. Guinier-type plots (ln$I(q)$ vs. q^2) for TCBQ-impregnated activated carbon electrodes prepared using (a) Sample 1, (b) Sample 2, (c) Sample 3, (d) Sample 4, (e) Sample 5, and (f) Maxsorb®. The dashed lines represent the linear least-squares fits applied over the selected high-q region used to generate apparent d values in the TCBQ series. The apparent R_{app}-like parameters and apparent d descriptors are summarized in **Table S6**.

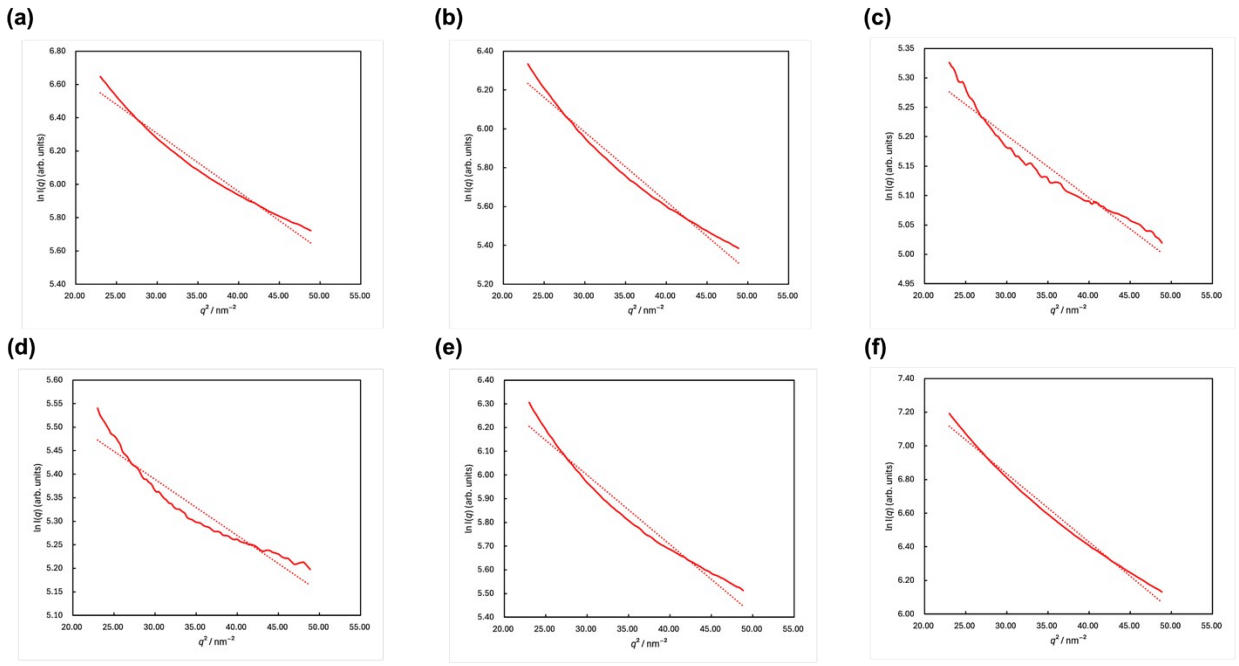

Fig. S9. Guinier-type plots (lnI(q) vs. q^2) for DCAQ-impregnated activated carbon electrodes prepared using (a) Sample 1, (b) Sample 2, (c) Sample 3, (d) Sample 4, (e) Sample 5, and (f) Maxsorb®. The dashed lines represent the linear least-squares fits applied over the selected high-q region used to generate apparent d values for the DCAQ series. The apparent R_{app}-like parameters and apparent d descriptors are summarized in **Table S6**.